Enhanced photocatalytic hydrogen generation with Pt Nanoparticles on multi-phase polycrystalline microporous MnO$_2$ photocatalyst

Yi-Hao Pai*, Chih-Teng Tsai, Su-Yun Fang

Department of Opto-Electronic Engineering, National Dong Hwa University, No. 1, Sec. 2, Da Hsueh Rd., Shoufeng, Hualien 97401, Taiwan, ROC

HIGHLIGHTS

► The Mn–O functional groups can be obtained by tuning the precursor concentrations.
► Multi-phase polycrystalline microporous MnO$_2$ show superior photocatalytic activity.
► Hydrogen production rate can be promoted in the presence of the MnO$_2$ photocatalyst.
► The use of macroporous MnO$_2$ photocatalyst can effectively inhibit CO poisoning.

ARTICLE INFO

ABSTRACT

A multi-phase polycrystalline microporous manganese dioxide (MnO$_2$) photocatalyst for light-induced water splitting and hydrogen generation is performed via a redox reaction under various hydrothermal conditions. By tuning the precursor concentrations down to 0.1 M, two kinds of Mn–O functional groups, including pyrolusite structures at 416, 433, 455, 609 and 646 cm^{-1} and ramsdellite structures at 466 and 576 cm^{-1}, can be obtained by FT-IR. Morphological and phase characterizations are also examined by FE-SEM and XRD techniques, respectively. A series of peaks, corresponding to planes (110) and (200) of our sample can be indexed as a β-MnO$_2$ crystal with a corresponding lattice spacing of 3.11 Å and 2.19 Å. In particular, a significant enhancement of light-induced hydrogen generation by water splitting has been observed at a Pt–MnO$_2$/C photocatalyst with an optimum hydrogen generation rate of 2261 μ mol g^{-1} h^{-1} due to the improvement of electro-oxidation of methanol aqueous solutions, compared to a Pt–TiO$_2$/C photocatalyst. The photoelectrochemical measurement also indicates that the multi-phase polycrystalline macroporous MnO$_2$ photocatalyst can indeed effectively inhibit CO poisoning, help CO re-oxidation in the cocatalyst surface and maintain the catalyst's surface area in methanol oxidation and hydrogen generation efficiency.

1. Introduction

The photochemical hydrogen production technology, a popular clean energy technology in recent years, would not have been possible without the significant breakthrough made by Fujishima and Honda, two scholars of the University of Tokyo, Japan; their research on photocatalyst materials in 1972 made the application of light energy in hydrogen production feasible [1]. So far, the key to photochemical hydrogen production lies in the preparation and selection of photocatalyst materials. Generally, the reaction principle is to irradiate semiconductor materials with light energy greater than the band gap to stimulate the redox ability of electron–hole pairs into conducting redox reactions. More specifically, the band distribution of the selected semiconductor materials must conform to the reduction potential of water. Also, the literature proposes that only transition metal oxides with d^0 or d^{10} electronic configuration have a photochemical activity high enough to split water into H$_2$ and O$_2$ [2–4]. More specifically, adding metal particles (such as Pt, Au, etc.) or metal oxide catalysts (NiO or RuO$_2$) greatly enhances the photocatalytic activity of materials [5,6]. The main attribution to the changed electron configuration is the additive, which effectively prevents the phenomenon of electron–hole recombination.

Because the layered manganese dioxide (MnO$_2$) nanostructures allow protons to be conducted in electrolytes without restructuring, they have an outstanding electrochemical performance among catalyst materials [7,8]. Rebello et al. used electrodes containing MnO$_x$ to study the performance of direct-methanol fuel cells; the

* Corresponding author. Tel./fax: +886 3 8634195.
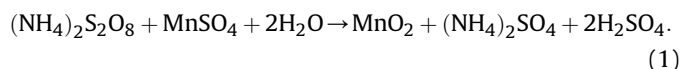 E-mail address: paiyihao@mail.ndhu.edu.tw (Y.-H. Pai).

results indicated that in addition to having an octahedral molecular structure, synthetic MnO_x had strong electrochemical oxidation activity in methanol decomposition [9]. The report by Zhao et al. also pointed out that the preparation of manganese dioxide electrodes using the anodic deposition technique improved the electrochemical performance and inhibited the electrodes for co-tolerance [10]. However, few studies have explored the synthesis of the porous manganese dioxide photocatalyst and tested its efficiency in photochemical hydrogen production. In particular, the long-term stability of hydrogen production has yet to be assessed.

This study used hydrothermal synthesis to synthesize the microporous manganese dioxide photocatalyst material, and the FTIR system to understand the relationship between the process parameters and molecular bonding in order to find the optimal process conditions. In addition, this study explored the crystallization characteristics of the optimized microporous manganese dioxide photocatalyst material. To understand the differences between the microporous manganese dioxide photocatalyst and the industrial-grade titanium dioxide photocatalyst materials in the photoelectrochemical hydrogen production performance, this study added Pt as a cocatalyst in order to compare the electrochemical and photoelectrochemical activities. Finally, via the photochemical hydrogen production system in the setting of an aqueous solution containing 1 M methanol, an efficiency test on the hydrogen production and assessment of its long-term stability were conducted.

2. Experimental procedure

2.1. Preparation of microporous MnO_2 and MnO_2-supported Pt photocatalytic powders

A manganese precursor with a general formula, $MnSO_4$ and $(NH_4)_2S_2O_8$ from the ECHO CHEMICAL CO. LTD. was first mixed to achieve three precursor concentrations of 0.1 M (for Sample A), 0.3 M (for Sample B) and 0.5 M (for Sample C) of aqueous solution under an ultrasonic mixing technique [11] at room temperature. An equal volume of the obtained precursor solution was injected into quartz glassware and thereafter, mounted in a Teflon clip. A hydrothermal synthesis, with an optimum reaction temperature of 160 °C for 1 h, was utilized for the preparation of microporous MnO_2 photocatalytic powder [12], which caused a reaction:

$$(NH_4)_2S_2O_8 + MnSO_4 + 2H_2O \rightarrow MnO_2 + (NH_4)_2SO_4 + 2H_2SO_4. \tag{1}$$

Afterward, 1.5 g of microporous MnO_2 photocatalytic powder was first dispersed into 700 ml of ethanol by using a sonochemical mixing technique. Subsequently, an aqueous solution containing $H_2PtCl_6 \cdot 6H_2O$ (Seedchem Company PTY. LTD) was added to the above mixed solutions. Finally, a 1.0 wt.% Pt cocatalyst on microporous MnO_2 supports was performed by using an impregnation method at 80 °C for 2 h. The solid precipitates were washed and filtered with distilled water, and then dried in a vacuum oven at 70 °C. To further realize the results of photocatalytic activity for MnO_2-supported Pt photocatalytic powders, an equal amount of Pt cocatalyst on industrial TiO_2 photocatalytic powders (United Associate Co. Ltd.) was prepared for comparison.

2.2. Characterization and optoelectrochemical properties of MnO_2-supported Pt photocatalyst

The surface chemical content and compositional bonds of microporous MnO_2 photocatalytic powders were analyzed using a Varian 640 FT-IR Spectrophotometer (Varian, Australia). The structural properties of the microporous MnO_2 photocatalytic powders were measured with a conventional X-ray diffractometer (XRD, MAC Science M21X) using Cu K_α radiation ($\lambda = 1.54$ Å). Field Emission Scanning Electron Microscopy (FE-SEM, JEOL-6700F) was employed to accurately characterize the Pt cocatalyst and dispersion of the microporous MnO_2 photocatalytic supports. Elementary identification was performed by using an energy-dispersive X-ray spectroscope (EDXS, HORIBA EMAX).

To realize the electroactivities and optoelectrochemical properties of the microporous MnO_2 photocatalyst, 0.05 ml of catalyst ink (containing 5 wt.% Nafion solution (DuPont) and carbon black as a conductive agent) was loaded onto a glassy carbon disk electrode (diameter of the active zone was 3 mm). After drying, the electrochemical and optoelectrochemical properties of the physically mixed Pt–MnO_2/C photocatalysts were measured by Cyclic Voltammetry (CV) through a CHI614D electrochemical analyzer in a deaerated aqueous solution of 1 M H_2SO_4 with a 50 mV s^{-1} scanning rate between −0.4 and 1.2 V. This was conducted at room temperature under 300-W white light lamp (Phillips) irradiation and simultaneously compared with a Pt–TiO_2/C and Pt/C electrode (a Pt wire serving as the counter electrode and Ag/AgCl serving as the reference electrode). Furthermore, the electrocatalytic activity of the electrodes toward electrooxidation of methanol was examined in a deaerated aqueous solution of 1 M H_2SO_4 solution containing 1 M methanol.

2.3. Photochemical hydrogen generation test

The photocatalytic reaction was performed in a reactor equipped with a cooling water jacketed cylindrical quartz cell. A 300 W white light lamp was mounted outside the above cell. The photocatalytic hydrogen evolution of water splitting was carried out in 150 ml aqueous methanol solution (vol. ratio of MeOH: H_2O = 1:9) containing of 0.3 g photocatalytic powders at temperature of 50 °C. A reactive gas was collected over water in a gas jar. In more detail, the setup for the collection of a gas over water involves a container in which the reaction takes place and a gas collection container filled with water. Finally, a gas chromatography (China Gas Chromatography 9800) with a packed column (MS-5A, 3.5 m in length) and thermal conductivity detector was employed to analyze the gas generation.

3. Results and discussion

3.1. Characterization of multi-phase polycrystalline microporous MnO_2 photocatalyst

In order to find the optimal process conditions and to understand the variation of bonding and strength in precursor concentrations of the manganese dioxide functional group, this study used FTIR to observe the functional configuration of manganese dioxide for precursor concentrations, which are respectively 0.1 M, 0.3 M, and 0.5 M, as shown in Fig. 1. The prepared manganese dioxide photocatalyst had two kinds of Mn–O bonding structures: pyrolusite and ramsdellite. The functional group structure of the pyrolusite, with wavenumbers 416, 433, 455, 609, and 646 cm^{-1}, was that of an octahedron; the functional group structure of the ramsdellite, with wavenumbers 466 and 576 cm^{-1}, comprised of two main octahedra [12]. However, the change of precursor concentrations from 0.1 M to 0.5 M weakened the strength of the functional groups with wavenumber positions corresponding to those of pyrolusite and ramsdellite, which meant that the concentration of Mn–O molecules had no significant increasing trend. In other words, enhancing the precursor concentration cannot effectively increase the bond concentration of the Mn–O
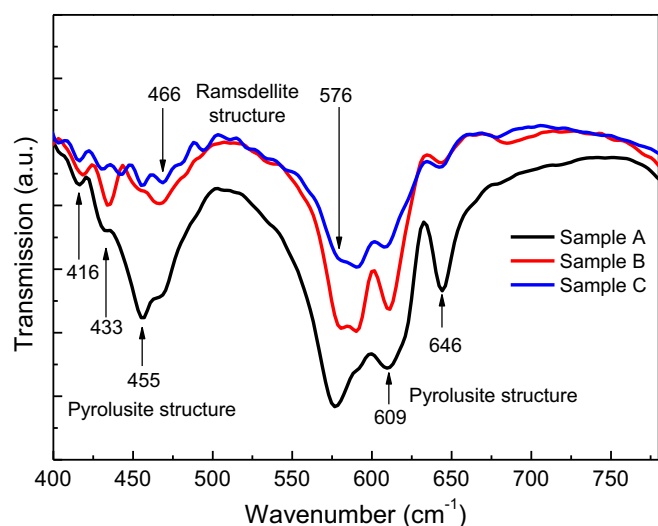
Fig. 1. FTIR analysis of the macroporous MnO_2 photocatalyst under various synthesis conditions.

molecule. Therefore, the best condition for synthesis is the precursor concentration of 0.1 M. This result is consistent with the process conditions described in the literature [13].

Fig. 2 shows how X-ray powder diffraction was used to observe the crystal structure of MnO_2 photocatalyst powder prepared by the precursor concentration of 0.1 M. In accordance with the Joint Committee on Powder Diffraction Standards (JCPDS) card (24-0735, 44-0141, 24-0734, and 14−0644), Fig. 2(a) shows the main angles of β-MnO_2 crystal to be 28.68° and 40.28°, which correspond to the diffraction surfaces of (110) and (200) respectively. When the angles of Mn_3O_4 crystals were 32.54°, 36.06°, and 45.64°, they corresponded to the diffraction surfaces of (103), (211), and (220) respectively. The figure also reveals diffraction peaks in the α and γ crystalline phases. Overall, with the precursor concentration of 0.1 M, the prepared manganese dioxide photocatalyst possessed the multi-phase polycrystalline structure of α, β, γ, and Mn_3O_4.

In order to understand the differences between the photocatalytic properties of the manganese dioxide photocatalyst materials and those of the widely used industrial-grade titanium dioxide photocatalyst, this study also conducted the crystal structure analysis of the photocatalyst materials; Fig. 2(b) shows the results. Like the JCPDS card, the titanium dioxide powder has two kinds of crystal structures: anatase and rutile. The main diffraction surfaces of the anatase are (101), (004), (200), (105) and (211), and those of the rutile are (110), (200), (111), and (210). The crystalline phase is identical to the synthetic structure mentioned in the literature [14].

In addition, this study modeled the catalyst design of Shi et al. Platinum catalyst nanoparticles were deposited on the surface of both photocatalyst materials, mainly because the deposited platinum nanoparticles are conducive to photocatalytic decomposition of the methanol solution [15]. According to a study by Lin et al., adding Pt, Au, or other metal catalyst particles to $KTiNbO_5$ photocatalyst material can also effectively improve its catalytic activity, which attributes to an efficient charge transfer process for the shift from the $KTiNbO_5$ surface to the precious metal catalyst particles, thereby reducing the electron−hole composite [16–18]. The result also shows that the precious metal nanoparticles are capable of serving as the hydrogen production activity center and enhancing the charge separation effect of the photocatalyst.

Fig. 3(a) shows the Pt−MnO_2 and Pt−TiO_2 photocatalyst materials with the Pt active metal catalyst particles added, and Fig. 3(b)
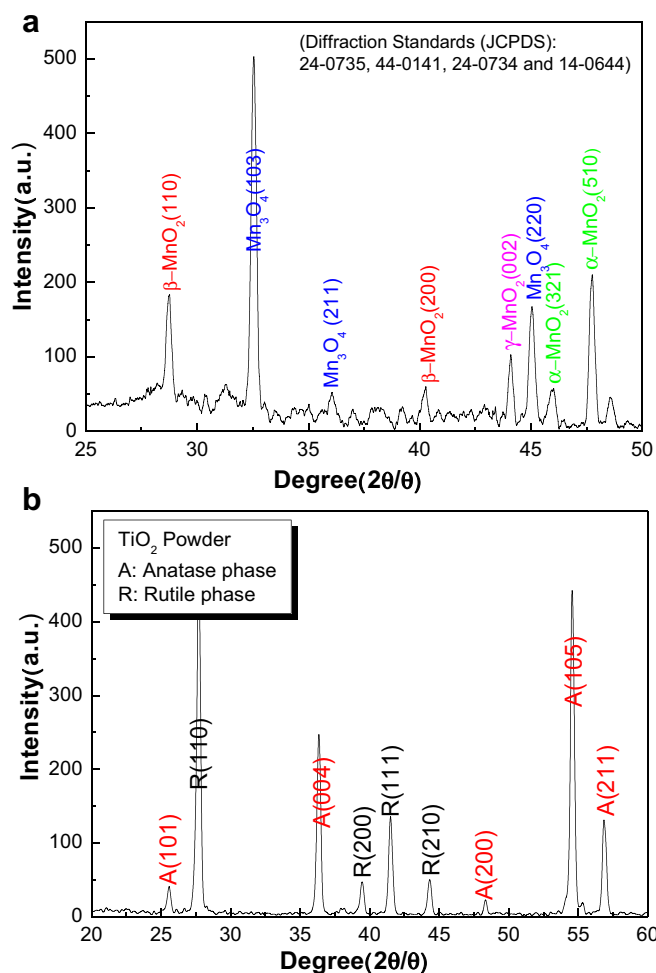

Fig. 2. The wide angle XRD spectra of the multi-phase polycrystalline macroporous (a) MnO_2 and (b) TiO_2 photocatalyst.

shows the secondary electron image of the surface morphology observed by the scanning electron microscopy. The gray area indicates the photocatalyst materials, and the bright white area indicates the platinum catalyst. The scattering caused by the electron beam on the different atomic numbers serves as the main basis for comparison. Both figures show the even dispersion of platinum electrode catalyst on the carrier surface, and the average particle size distribution ranges from a few nanometers to tens of nanometers. In Fig. 3(a) and Fig. 3(b), the results of the qualitative analysis conducted on the catalysts using the energy dispersive X-ray spectroscopy showed significant energy signal intensity in the excited state of the O, Pt, and Mn elements in the Pt−MnO_2 photocatalyst and in the excited state of the O, Pt, and Ti elements in the Pt−TiO_2 photocatalyst.

3.2. Photoelectrochemistry of multi-phase polycrystalline microporous MnO_2 photocatalyst

Fig. 4(a) is a diagram of the cyclic voltammetry measurements and analysis conducted for the above two electrode materials in conditions without light. The figure shows the Pt−MnO_2/C photocatalyst has significantly larger H^+ adsorption characteristic signals in the potential region ranging from −0.2 V to −0.1 V, which corresponds to the maximum current value of approximately −1.5 mA (compared to the Pt/C electrode of Pt−TiO_2/C). Furthermore, in H_2
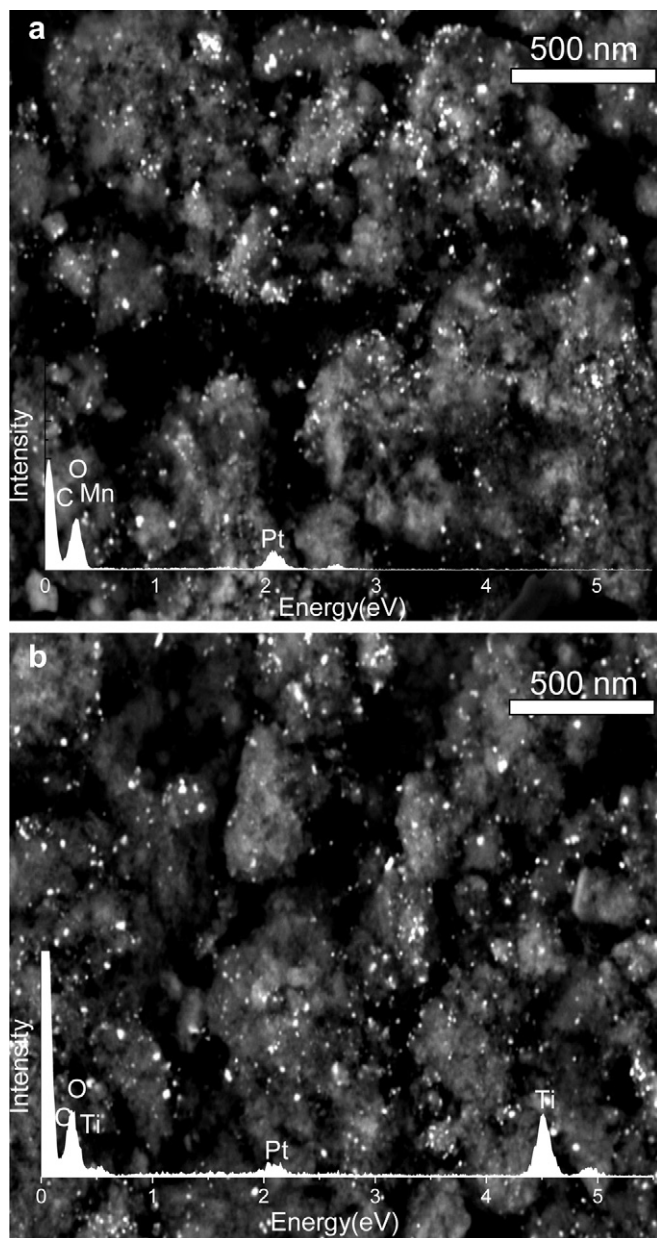
Fig. 3. The SEM images of the (a) Pt/MnO$_2$/C and (b) Pt/TiO$_2$/C electrode. (Inset: EDXS analysis for the photocatalytic electrode.)

Fig. 4. Cyclic voltammograms (at 50 mV s^{-1}, in 1 M H$_2$SO$_4$ aqueous solution) of the Pt/C electrode, the Pt/MnO$_2$/C electrode and Pt/TiO$_2$/C electrode measured in dark and under a broadband light source illuminations.

desorption potential, the maximum hydrogen desorption currents of Pt−MnO$_2$/C, Pt−TiO$_2$/C, and Pt/C photocatalyst electrodes correspond to the potentials of −0.25 V, −0.21 V, and −0.18 V respectively. This means that both Pt−MnO$_2$/C and Pt−TiO$_2$/C electrodes need a larger potential to conduct H$_2$ desorption, mainly because the MnO$_2$ and TiO$_2$ photocatalyst addition will cause the Pt−C catalyst impedance to rise. In addition to needing a larger potential for electrons to overcome the activation barrier in the transfer process, this change also directly affects the conduction properties of the protons in the electrochemical process. Fig. 4(b) is a diagram of the cyclic voltammetry measurements and analysis carried out under 500 W white light. The illustrations are the three-pole photo-electrochemical measurement schematic diagram and the photo-electrochemical system photos under 500 W white light. Under the lighting condition, the Pt−C catalyst was clearly not a photocatalyst material, so it did not produce any significant photoelectrochemical
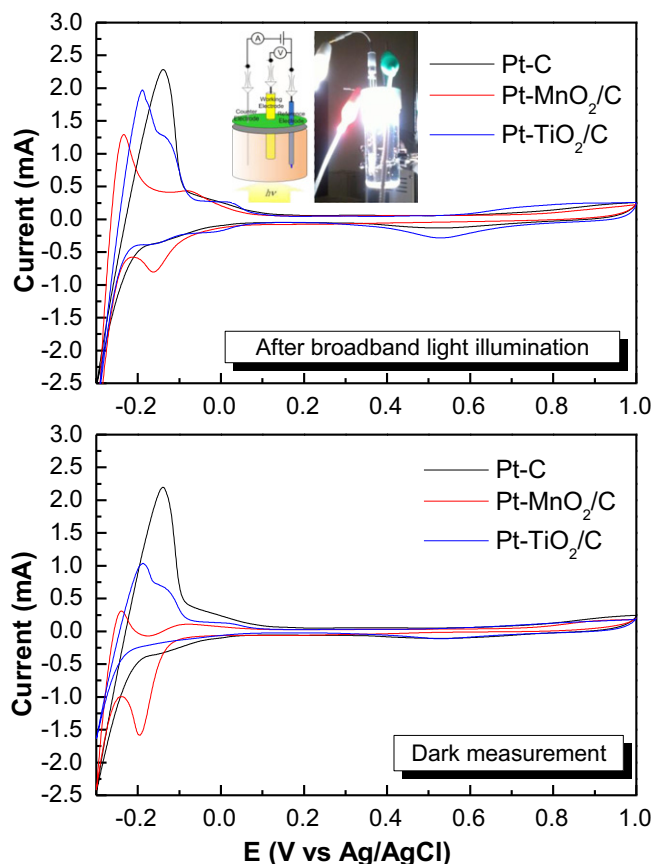
difference (compared with pre-lighting). Relatively, Pt−MnO$_2$/C and Pt−TiO$_2$/C electrodes with photocatalytic characteristics under this condition highlighted significant photoelectrochemical activity. In particular, compared to the non-illuminated conditions, the increased hydrogen adsorption and desorption areas were more obvious, and the average margins of the Pt−MnO$_2$/C and Pt−TiO$_2$/C electrodes rose by 1.8 times and 2.3 times respectively. According to the literature, the electrochemical active surface area Sact (cm^2 mg^{-1}) can be written as Q_H/Q_H^0, in which Q_H^0 is the charge (210 μC cm^{-2}) carried when the monolayer hydrogen is adsorbed on the platinum surface, and Q_H is the effective charge transfer [19,20] caused by hydrogen adsorption and desorption on the electrode surface. Overall, the effective catalytic activity areas of Pt−MnO$_2$/C and Pt−TiO$_2$/C electrodes under lighting conditions are 101.6 cm^2 mg^{-1} and 143.33 cm^2 mg^{-1} respectively.

3.3. Light-induced water splitting and hydrogen generation

To better understand the actual efficiency of Pt−MnO$_2$/C in hydrogen production, this study used the photocatalyst cracking methanol aqueous solution system for the measurement of the hydrogen production efficiency and at the same time carried out comparison with the Pt−TiO$_2$/C photocatalyst. As Fig. 5(a) shows, the system includes five parts: methanol aqueous solution in optical-fiber photoreactor; drainage and gas gathering system; temperature control system; cooling system; and lighting system. Fig. 5(b) is a spectral intensity diagram of the white lighting system. Fig. 5(c) is an entity photo diagram of the system in operation. The experimental results show that under the same test conditions, the
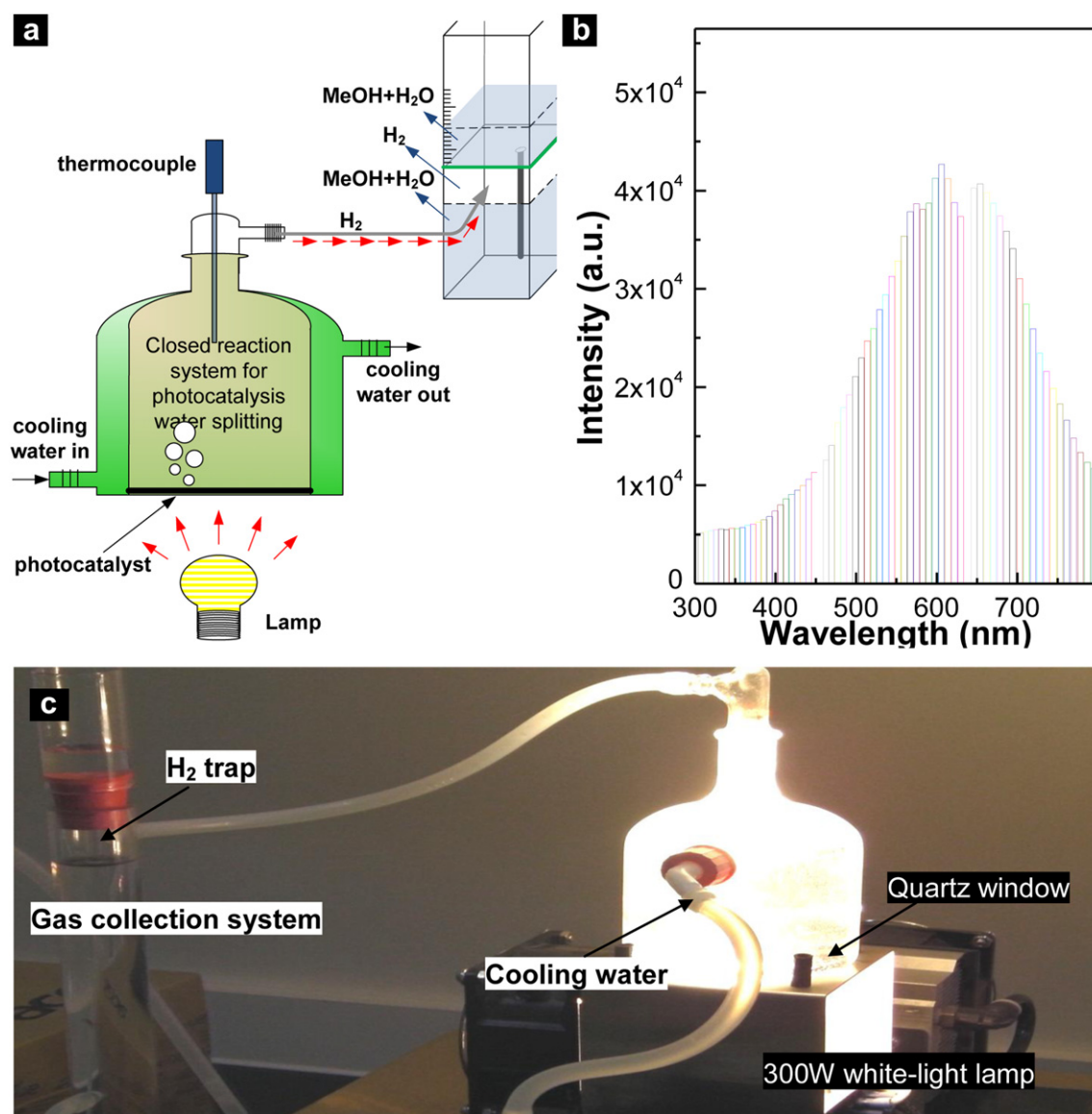
Fig. 5. (a) Scheme of closed reaction system for photocatalysis water splitting, (b) the emission spectrum of 300 W white-light lamp and (c) the photoelectrolysis cell setup with a collimated light beam passed through a quartz window to illuminate a photocatalyst layer.

hydrogen production rate of Pt–MnO$_2$/C photocatalyst is 2261 μ mol g^{-1} h^{-1}, while the photocatalytic hydrogen production rate of Pt–TiO$_2$/C is 1843 μ mol g^{-1} h^{-1}. The actual results of the comparison of the two electrodes' hydrogen production rates were contrary to expectations, especially the expectation that the aqueous methanol environment would not have a better hydrogen production rate due to the higher catalytic activity area (compared with the photoelectrochemical test results).

Fig. 6 shows a comparison chart for hydrogen yield versus time in the use of Pt–MnO$_2$/C and Pt–TiO$_2$/C photocatalysts in the setting of the methanol aqueous solution. Hydrogen production immediately stops when the light source is turned off (dark region); otherwise, hydrogen production continues. The entire operation was repeatedly carried out for four times. When using the Pt–MnO$_2$/C photocatalyst for photocatalytic production, no significant passivation was generated for the catalyst under the conditions of this repeated operation. The cumulative hydrogen production was more than 3800 μ moles after 2 h. However, in comparison with the Pt–TiO$_2$/C photocatalyst, the change in slope of the hydrogen yield versus time

decreased with the growth of hydrogen production time. Although the methanol in this reaction acts as an efficient hole scavenger and plays the role of inhibiting the charge recombination of the entire water cracking process [16,21], it will also produce effects not conducive to the catalyst, such as CO poisoning caused by the CO adsorbed on the Pt surface [22,23]. More specifically, methanol can be easily adsorbed on the Pt surface and through reaction (Pt + CH$_3$OH → Pt-COad + for 4H$^+$ + 4e$^-$) produce CO adsorption on Pt surface; while Pt can produce strong bonds with CO, making it difficult to desorb (the adsorption force between CO and Pt is about 180 kJ mol^{-1}). This results in CO occupying the Pt surface, gradually reducing the activity of the catalytic reaction and thus decreasing the efficiency of hydrogen production. Although the literature mentions that catalyst particles, such as Pt, Au, Cu, NiO, and so on, can effectively enhance the efficiency of hydrogen production [5,16], the impact of hydrogen production environment with sacrificial reagent on catalytic particles has rarely been explored. Therefore, in order to understand the impact of methanol aqueous solution on photocatalyst materials in the hydrogen production process, this
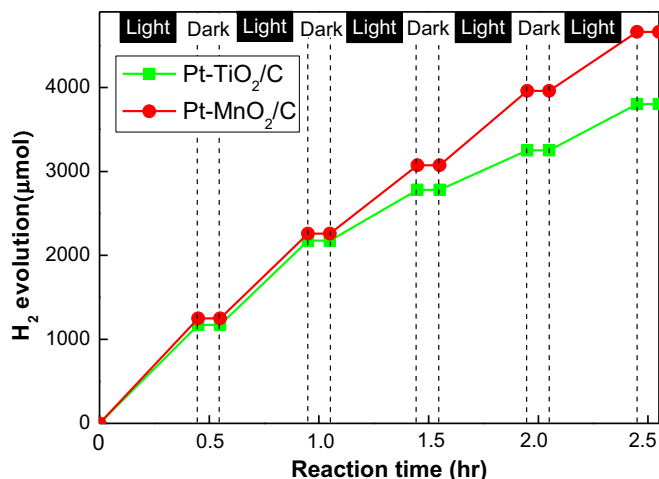
Fig. 6. Time course of H_2 evolution on $Pt/MnO_2/C$ and $Pt/TiO_2/C$ catalysts under white-light irradiation (condition: 0.3 g powder catalyst, 100 ml aqueous methanol solution) (vol. ratio of MeOH: H_2O (1:9)).

study carried out electrochemical measurements of two photo-catalytic materials in 1 M sulfuric acid and 1 M methanol mixed aqueous solutions, as shown in Fig. 7. The figure shows that the Pt–MnO_2/C electrode has significant Methanol Oxidation Reaction (MOR) signal between potentials of 0.6 V–0.8 V; note that the stronger the MOR peak current signal is, the more oxidized the methanol molecules, resulting in more electrons transfers and thus a better catalytic performance. In addition, in the reverse scan process, only a weak current signal was found in 0.45 V vicinity. According to the literature [24], the porous texture of nano-MnOx allows methanol molecules to reach the active Pt surface sites and undergo oxidation. It is presumed that nano-MnOx acts as an oxygen supplier to the adsorbed intermediates facilitating its oxidation to CO_2. Compared to the Pt–TiO_2/C photocatalyst electrode, the same significant MOR peak signal appeared between the potentials of 0.6–0.8 V. However, in the reverse scan process, the significant peak signal appeared near 0.45 V, which attributed to the methanol being not fully oxidized in the oxidation process and thus causing the catalyst metal surface to adsorb CO or other intermediates [25]. The result also shows that the CO or other intermediates continued to accumulate on the catalyst surface, which caused CO poisoning of the catalyst and made the catalyst lose activity centers to react with

methanol, thereby decreasing catalytic performance. In addition, to determine the CO tolerance ability of the catalyst by the ratio of the forward peak current (I_f) to the reverse peak current (I_b) (note: the higher the ratio, the better the CO tolerance ability will be), we can see that the value of the Pt–TiO_2/C photocatalyst electrode is 1.1, which is lower than the 4.6 value of the Pt–MnO_2/C photocatalyst electrode. This result also indicates that the use of multi-phase polycrystalline macroporous MnO_2 photocatalyst can indeed effectively inhibit CO poisoning, assist CO re-oxidation in the catalyst surface, and maintain methanol oxidation in the catalyst surface area and hydrogen production efficiency.

4. Conclusions

A bifunctional, multi-phase polycrystalline microporous MnO_2-supported Pt photocatalyst for hydrogen generation by water splitting was demonstrated by the hydrothermal synthesis method. The vibrational spectroscopic results showed that the microporous MnO_2-supports prepared with a precursor concentration of 0.1 M had two kinds of Mn–O bonding structures containing pyrolusite structures at 416, 433, 455, 609 and 646 cm^{-1} and ramsdellite structures at 466 and 576 cm^{-1}. Characterizations from the XRD also reveal the diffraction surfaces of a β-MnO_2 crystal as (110) and (200), which correspond to the lattice spacing of 3.11 Å and 2.19 Å, respectively. By comparing the catalytic activity, the effective catalytic activity areas of Pt–MnO_2/C and Pt–TiO_2/C electrodes under lighting conditions are 101.6 $cm^2\,mg^{-1}$ and 143.33 $cm^2\,mg^{-1}$, respectively. However, the Pt–MnO_2/C photocatalyst from an aqueous methanol solution under white-light irradiation possessed a higher hydrogen generation rate of 2261 μ mol $g^{-1}\,h^{-1}$ than Pt–TiO_2/C with 1843 μ mol $g^{-1}\,h^{-1}$, which can be attributed to the effective CO tolerance of the Pt–MnO_2/C photocatalyst. Furthermore, the photoelectrochemical measurements of two photo-catalytic materials in 1 M sulfuric acid and 1 M methanol mixed aqueous solutions were confirmed so that the multi-phase poly-crystalline macroporous MnO_2 photocatalyst could indeed effectively inhibit CO poisoning and help CO re-oxidation on the cocatalyst surface.

Acknowledgments

References

[1] A. Fujishima, K. Honda, Nature 238 (5358) (1972) 37–38.
[2] K. Sayama, K. Mukasa, R. Abe, Y. Abe, Y. Abe, H. Arakawa, J. Photochem. Photobiol. A 148 (2002) 71–77.
[3] D.W. Hwang, H.G. Kim, J. Kim, K.Y. Cha, Y.G. Kim, J.S. Lee, J. Catal. 193 (2000) 40–48.
[4] Z.B. Lei, G.J. Ma, M.Y. Liu, W.S. You, H.J. Yan, G.P. Wu, T. Takata, M. Hara, K. Domen, C. Li, J. Catal. 237 (2006) 322.
[5] H.Y. Lin, H.C. Yang, W.L. Wang, Catal. Today 174 (2011) 106–113.
[6] M.K. Tian, W.F. Shangguan, J. Yuan, L. Jiang, M.X. Chen, J.W. Shi, Z.Y. Ouyang, S.J. Wang, Appl. Catal. A 309 (2006) 76–84.
[7] H. Zhang, G.P. Cao, Z.Y. Wang, Y.H. Yang, Z.J. Shi, Z.N. Gu, Nano Lett. 8 (2008) 2664.
[8] O. Ghodbane, J.L. Pascal, F. Favier, ACS Appl. Mater. Interfaces 1 (2009) 1130.
[9] J.S. Rebello, P.V. Samant, J.L. Figueiredo, J.B. Fernandes, J. Power Sources 153 (2006) 36–40.
[10] G.-Y. Zhao, H.-L. Li, Appl. Surf. Sci. 254 (2008) 3232.
[11] Y. Han, S. Li, X. Wang, I. Bauer, M. Yin, Ultrason. Sonochem. 14 (2007) 286.
[12] T. Gao, H. Fjellvag, P. Norby, Nanotechnology 20 (2009) 055610.
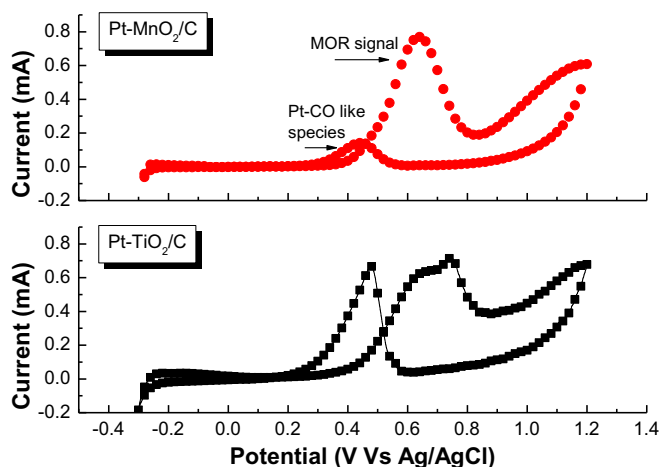[13] Y.K. Hsu, Y.C. Chen, Y.G. Lin, L.C. Chen, K.H. Chen, Chem. Commun. 47 (2011) 1252–1254.

Fig. 7. CVs for methanol electro-oxidation at $Pt/MnO_2/C$ and $Pt/TiO_2/C$ electrodes in 1 M HSO_4 containing 1 M methanol (Potential scan rate: 20 mV s^{-1}).

[14] Y. Li, H. Yu, W. Song, G. Li, B. Yi, Z. Shao, Int. J. Hydrog. Energy 36 (22) (2011) 14374—14380.

[15] J. Shi, J. Chen, Z. Feng, T. Chen, Y. Lian, X. Wang, C. Li, J. Phys. Chem. C 111 (2007) 693—699.

[16] H.Y. Lin, Y.S. Chang, Int. J. Hydrog. Energy 35 (2010) 8463—8471.

[17] A.L. Linsebigler, G. Lu, J.T. Yates Jr., Chem. Rev. 95 (1995) 735—758.

[18] K. Iwata, T. Takaya, H. Hamaguchi, A. Yamakata, T.A. Ishibashi, H. Onishi, J. Phys. Chem. B 108 (2004) 20233e9.

[19] Y.H. Pai, C.W. Tseng, J. Power Sources 202 (2012) 28—34.

[20] Y. Xing, J. Phys. Chem. B 108 (2004) 19255.

[21] A. Yamakata, T.A. Ishibashi, J. Onishi, J. Phys. Chem. B 107 (2003) 9820e3.

[22] X. Tang, B. Zhang, Y. Li, Y. Xu, Q. Xin, W. Shen, Catal. Today 93 (2004) 191.

[23] C. Wang, M. Waje, X. Wang, J.M. Tang, R.C. Haddon, Y. Yan, Nano Lett. 4 (2004) 345—348.

[24] M.S. El-Deab, Int. J. Electrochem. Sci. 4 (2009) 1329—1338.

[25] X. Zhang, K.Y. Chan, Chem. Mater. 15 (2003) 451—459.